

Modeling O-Star X-Ray Emission-Line Profiles:  
Fitting a Parameterized, Spherically-Symmetric Wind  
Model to *Chandra* Spectra

Swarthmore College Senior Thesis in Astrophysics  
*Swarthmore College Department of Physics and Astronomy,  
500 College Ave., Swarthmore PA 19081*

Roban Hultman Kramer

`roban@sccs.swarthmore.edu`

<http://www.sccs.swarthmore.edu/~roban/>

advisor: David H. Cohen

## Abstract

X-ray emission from hot (O- and B-type) stars is a long-standing astrophysical puzzle. High-resolution x-ray spectroscopy of hot stars resolves emission line profile shapes, offering direct insight into the dynamics and spatial distribution of the x-ray-emitting plasma. The O supergiant  $\zeta$  Puppis shows broad, blueshifted, and asymmetric line profiles, generally consistent with the wind-shock picture of OB star X-ray production. Here, for the first time, this is demonstrated quantitatively by fitting a spherically-symmetric phenomenological wind model to a *Chandra* spectrum of  $\zeta$  Puppis. The results of the fits to eight lines are presented here. Statistically good fits to seven of the lines are achieved, with extracted parameters providing constraints on the amount of absorption in the wind and the minimum radius of x-ray emission. The results indicate that a modest amount of wind attenuation is required, which is inconsistent with previous theoretical calculations of continuum optical depths. The implications of these results are discussed in light of other recent observational and theoretical work.

## 1. Introduction to hot star winds

All stars exchange material with their environments through accretion disks, supernovae, mass transfer in close binaries, stellar winds and other processes. In most stars, at least until the end stages of stellar evolution, a wind is the predominant mass-loss process, and can remove enough material to significantly decrease the mass of the star. O stars, though relatively rare, play an important role in star-forming regions, being the first to form, and the fastest-evolving and most luminous objects in such regions. O-star winds can have high kinetic energy and momentum fluxes and may play important roles in shock formation, turbulence in, and enrichment and dispersal of, star-forming clouds, and triggered star formation.

This thesis will detail the first effort to perform quantitative, statistical fits on x-ray emission line profiles from hot star winds. This work involves fitting a simple, spherically-symmetric wind model and extracting the values of three model parameters with important physical implications.

### 1.1. Radiation-driven winds

All O stars (and early B stars) have radiatively-driven winds, meaning the wind is propelled primarily by radiation pressure rather than by a gas pressure gradient as in the winds of cooler stars like the sun. To accelerate a massive wind out of the gravitational potential well, energy and momentum must be efficiently transferred from the star’s radiation field to the wind material. This type of outflow is often referred to as a “line-driven wind” because line opacity dominates the absorption and scattering processes that effect the transfer.

The basic process of momentum transfer is bound absorption followed by spontaneous emission. Consider an atom of mass  $m$  with a transition at rest frequency  $\nu_0$ , and a momentum component along a particular direction  $mv_r$ . The atom can absorb a photon moving in that direction if it is of frequency  $\nu_1 = \nu_0(1 + v_r/c)$ , changing the atom’s momentum to  $mv'_r = mv_r + h\nu_1/c = mv_r + (h\nu_0/c)(1 + v_r/c)$ . If the subsequent emission is isotropic, we would expect that, on average, it will not change the atom’s momentum. This can easily be shown by considering a photon emitted at an arbitrary angle  $\phi$  to the original direction with frequency  $\nu_2 = \nu_0(1 + v'_r/c)$  and momentum along the original direction  $\cos\phi (h\nu_2/c)$ . For  $v_r \ll c$  and  $h\nu_0 \ll mc$ , the total change in the component of momentum along the direction of the incident photon is then

$$\Delta mv_r = (h\nu_0/c)(1 - \cos\phi) . \tag{1-1}$$

Assuming isotropic emission, the average change in momentum is then

$$\langle \Delta mv \rangle = (1/4\pi) \int_{-\pi/2}^{\pi/2} (h\nu_0/mc)(1 - \cos\phi) 2\pi \sin\phi d\phi = h\nu_0/c, \tag{1-2}$$

which is the same as for the initial absorption event (with  $v_r \ll c$ ), as predicted (this derivation closely follows Lamers & Cassinelli 1999).

The ions in the wind that will interact most strongly with the radiation field will obviously be those with the strongest and most numerous transitions near the peak wavelength of the stellar spectrum. If the bulk of the wind material is to be accelerated, these ions will have to share momentum with the rest of the wind through Coulomb interactions. In some stars with very low-density winds the momentum sharing may be inefficient, in which case the wind would alter photospheric abundances by selectively removing certain elements (Babel 1995). This paper, however, will focus on high-density, O-star winds, in which momentum sharing is quite efficient.

An accelerating wind, by definition, consists of material at a range of velocities. The velocity dispersion in the wind increases the efficiency of the momentum transfer for optically thick lines by Doppler broadening the lines, which makes more of the stellar continuum available for line driving. Velocity dispersion can also increase the likelihood of “multiple scattering”, whereby a photon which has scattered off a particular line in one region of the wind may scatter off a different line in a different region of the wind if the relative velocity of the wind regions corresponds to the difference in wavelength of the two lines. This can be an important process in the winds of Wolf-Rayet stars (Owocki 2001).

Calculating the total acceleration of a wind is complicated by the sheer number of ions and transitions involved in the process and the interaction between the kinematics of the wind and the wavelength-space distribution of its opacity. Sobolev (1960) showed how to simplify the problem dramatically for a single line. Consider the reference frame of a particular comoving point in an expanding, accelerating wind. In this comoving frame all of the wind is moving away from the reference point, with increasing velocity farther from the point. Thus a photon emitted at the central frequency of a spectral line can only be absorbed in a limited region of the wind. As the photon travels farther from the emission point, the relative Doppler shift of the wind increases, shifting the line away from the photon’s frequency. If the width of the line can be characterized by a velocity  $v_{\text{line}}$  (which might be the thermal velocity, or include contributions from micro-turbulent broadening), the characteristic length beyond which a photon is unlikely to be absorbed is

$$l_{\text{Sob}} \equiv v_{\text{line}}/(dv/dr) , \quad (1-3)$$

where  $dv/dr$  is the velocity gradient of the wind. This is much smaller than the length scale of the velocity or density gradients  $v/(dv/dr) \approx |\rho/(d\rho/dr)|$ , since we expect  $v \gg v_{\text{line}}$ . This allows us to localize the problem of determining the optical depth  $\tau_\nu$  for a path from the photosphere to a point in the wind:

$$\tau \approx \kappa\rho l_{\text{Sob}} = \kappa\rho v_{\text{line}}/(dv/dr) , \quad (1-4)$$

where  $\kappa$  is the line opacity or mass absorption coefficient (which has dimensions of area per unit mass) and  $\rho$  the local mass density. It can then be shown using similar arguments (Owocki 2001) that the radiative acceleration due to scattering in a single line is simply

$$g_{\text{line}} \approx \frac{\kappa v_{\text{line}} \nu_0 L_\nu}{4\pi r^2 c^2} \left( \frac{1 - e^{-\tau}}{\tau} \right) . \quad (1-5)$$

Assuming each photon will scatter only once, the total acceleration of the wind is the sum of the contribution from each independent line in the wind,

$$v dv/dr = \sum_{\text{lines}} g_{\text{line}} - \frac{GM(1 - \Gamma_e)}{r^2} \quad \text{where} \quad \Gamma_e = \frac{\kappa_e L}{4\pi GMc}. \quad (1-6)$$

The last term accounts for gravity and acceleration due to free-electron scattering ( $\kappa_e$  is the free-electron opacity) (Owocki 2001). Solving this equation is complicated, since terms in the sum depend on the acceleration itself through the optical depth (Eqns. 1-4 and 1-5).

Castor, Abbott, & Klein (1975b) developed method for finding self-consistent solutions to this equation by treating the number of lines per unit opacity as a power law in the opacity  $dN/d\kappa \propto \kappa^{\alpha-2}$ . This gives the solution

$$v(r) = v_{\text{esc}} \sqrt{\frac{\alpha}{1 - \alpha}} \left(1 - \frac{R_*}{r}\right)^{1/2}, \quad (1-7)$$

where  $v_{\text{esc}}$  is the surface escape velocity and  $R_*$  is the stellar radius. Taking the angular extent of the stellar disk into account yields the more general form

$$v(r) = v_{\infty} \left(1 - \frac{R_*}{r}\right)^{\beta}, \quad (1-8)$$

with  $\beta$  (which is typically found, theoretically and observationally, to have a value  $\beta \approx 0.8$ ) describing how quickly the wind accelerates to its terminal velocity  $v_{\infty}$  (Owocki 2001; Lamers & Cassinelli 1999).

If we assume a constant mass-loss rate,  $\dot{M}$ , and a radially expanding wind, conservation of mass gives the following condition at all points in the wind:

$$\dot{M} \equiv \frac{dm}{dt} = \frac{dm}{dr} \frac{dr}{dt} = 4\pi r^2 \rho(r) v(r). \quad (1-9)$$

Assuming a velocity law with the form of Equation 1-8, we get density as a function of radius:

$$\rho(r) = \frac{\dot{M}}{4\pi r^2 v_{\infty} \left(1 - \frac{R_*}{r}\right)^{\beta}}. \quad (1-10)$$

Modern radiation-driven wind theory is generally considered quite successful (Howarth & Prinja 1996; Kudritzki & Puls 2000), though some comparisons with observationally determined mass-loss rates and terminal velocities have revealed discrepancies, particularly for dense winds (Leitherer & Lamers 1993; Lamers & Leitherer 1993). The next two subsections discuss some of the observational techniques used to study hot star winds and test the limits of current theoretical understanding.

## 1.2. Spectral wind diagnostics

The complicated interaction of the wind and stellar radiation leaves its signature in the stellar spectrum from the radio to the x-ray. The spectra can be used to determine many properties of the wind, the two most fundamental global properties being the mass-loss rate and the terminal velocity. Other important properties with spectroscopic signatures include wind variability, and density, velocity, and shock structure.

In the radio and IR, free-free emission in the wind forms a continuum excess superimposed on the photospheric spectrum. Mass-loss rate determinations from the free-free continuum rely on simpler models than other methods, so this is often considered the most reliable diagnostic of mass loss (Bieging, Abbott, & Churchwell 1989; Leitherer, Chapman, & Koribalski 1995). At shorter wavelengths,  $H_\alpha$  line emission can also be used to derive mass-loss rates (Puls et al. 1996). Since free-free emission is a two-body process and the  $H_\alpha$  emission arises primarily from recombination – also a two-body process, these are both “density-squared” diagnostics, depending on the product of electron and ion number densities. Thus, in the presence of clumping or other density inhomogeneities, systematic errors may be introduced into mass-loss rates determined using these methods (Lamers & Leitherer 1993).

Perhaps the most studied wind diagnostic is the “P-Cygni profile”. This distinctive line shape, usually seen in the UV, consists of a blue-shifted absorption trough blended steeply into a red-shifted emission line. The absorption trough, in particular, is used as a diagnostic of wind velocity structure (Prinja, Barlow, & Howarth 1990), ionization structure (Lamers et al. 1999), and mass-loss rate (Howarth & Prinja 1989). The depth of the absorption trough depends on column density, so this diagnostic is not as affected by density inhomogeneities as determinations that make use of density-squared processes. For massive winds, though, the trough can be saturated, which decreases the sensitivity to column density, but can actually be helpful in the determination of terminal velocities (Prinja et al. 1990).

This paper will focus on the O4f supergiant  $\zeta$  Puppis, located 0.45 kpc away in the Gum Nebula OB association. Basic stellar parameters are summarized in Table 1. Bieging et al. (1989) and Lamers & Leitherer (1993) used radio free-free emission to determine mass-loss rates, while Prinja, Barlow, & Howarth (1991) fit a model to the  $H_\alpha$  line profile. The x-ray luminosity determined by Sciortino et al. (1990) was based on *Einstein Observatory* data. The terminal velocity determination of Prinja et al. (1990) was based on observations of saturated P-Cygni profiles.

## 1.3. X-ray emission and absorption

When it was first observed that x-ray emission is commonly associated with hot stars (Seward et al. 1979; Harnden et al. 1979) there was no agreement on what mechanism produces

the emission. Some models invoked a corona as the repository of the hot, x-ray-emitting gas (Cassinelli & Olson 1979). Radiatively-driven, supersonic wind models had already been developed to explain the observed massive, high-speed winds of such stars (Lucy & Solomon 1970; Castor et al. 1975b). It was immediately recognized that the presence of wind material would affect the observed x-ray flux and spectral distribution, and the observed level of wind absorption made it difficult to explain the observed x-ray flux with a corona. Instead it was suggested that the large kinetic-energy flux carried by the wind might be able to generate the high-temperature gas necessary to explain the observed emission. Castor, McCray, & Weaver (1975a) had already proposed that winds from early-type stars could create “interstellar bubbles” bounded by an interaction region where the wind encounters the interstellar medium (a similar model of planetary nebulae formation was proposed by Kwok, Purton, & Fitzgerald 1978). Harnden et al. (1979), however, concluded that their observations required too low a wind column density for a coronal model and too high a source temperature for a wind interaction model.

Lucy & White (1980) were the first to suggest that shocks could be produced within the wind itself by instabilities in the line-driving force. Such instabilities would create numerous shock zones throughout the wind capable of explaining the observed x-ray flux. Variations on the wind-shock theme, invoking a variety of shock-generation mechanism have subsequently been developed (Lucy 1982; Mullan 1984; Owocki, Castor, & Rybicki 1988; MacFarlane & Cassinelli 1989; Chen & White 1991; Feldmeier, Puls, & Pauldrach 1997). The most recent variants of the wind-shock model invoke magnetic fields to channel ionized wind material into collisional shock zones (Gagné et al. 1997; Babel & Montmerle 1997; ud-Doula & Owocki 2002).

X-ray spectral resolution available before *Chandra* and *XMM* was not high enough to distinguish individual lines, so modeling focused on explaining the total x-ray luminosity and broad spectral distribution. Chlebowski, Harnden, & Sciortino (1989) and Sciortino et al. (1990) studied x-ray spectra of O stars observed by the *Einstein X-Ray Observatory*. They found that the x-ray luminosity  $L_x$  scales roughly with bolometric luminosity  $L_{\text{bol}}$ , with an average value of  $\log_{10}(L_x/L_{\text{bol}}) = -6.46$ , close to the previously established value for O stars of  $\log_{10}(L_x/L_{\text{bol}}) \approx -7$ . Sciortino et al. also found correlation between  $L_x$  and the wind momentum flux  $\dot{M}v_\infty$  and wind kinetic energy flux  $(1/2)\dot{M}v_\infty^2$ . This is not surprising since both these quantities correlate with  $L_{\text{bol}}$ , but the authors suggest these may be more fundamental, physical relationships.

In an attempt to find an additional correlation to explain the residual scatter in the  $L_x$ - $L_{\text{bol}}$  correlation, Kudritzki et al. (1996) studied *ROSAT* PSPC observations of 42 O stars. With no additional correlations, they found  $\log_{10}(L_x/L_{\text{bol}}) = -6.7 \pm 0.35$ . They were able to reduce the scatter using  $L_x \propto L_{\text{bol}}^{1.34}(\dot{M}/v_\infty)^{-0.38}$ , and suggest this is due to a correlation between the quantity  $\dot{M}/v_\infty$  and the volume filling factor of x-ray emitting gas in the wind, which in turn directly correlates with x-ray luminosity.

Owocki & Cohen (1999) used a series of simple analytical arguments about radiation transport in constant-velocity winds to derive the linear relationship between  $L_x$  and  $L_{\text{bol}}$ . They found

that  $L_x \sim (\dot{M}/v_\infty)^2$  for optically thin lines and  $L_x \sim (\dot{M}/v_\infty)^{1+s}$  for optically thick lines where the x-ray-emitting-gas volume filling factor  $f \sim r^s$ . From this relationship they could obtain the observed  $L_x \sim L_{\text{bol}}$  dependence only if  $-0.4 \lesssim s \lesssim -0.25$ .

Hillier et al. (1993) reported on a *ROSAT* spectrum of  $\zeta$  Puppis, testing the predictions of wind-shock models against the observations. Their model was based primarily on that of Owocki et al. (1988). Only a small fraction of the wind is assumed to be hot enough to emit x-rays. Most of the x-ray opacity comes from the cooler bulk of the wind, wherein arise the lower energy spectral signatures of the wind. Therefore, in order to model the observed spectrum, Hillier et al. calculated x-ray opacity in the wind from atmospheric models. They assumed x-ray emissivity scaled like density squared multiplied by a constant filling factor and used a slightly modified  $\beta$ -velocity law with  $\beta = 1$ . They also assumed that x-ray emission only “turns on” above a certain minimum radius  $R_{\text{min}}$ , based on line-driving models that suggest instabilities don’t develop immediately above the photosphere. By fitting one- and two-temperature models to the spectrum, they derived shock temperatures for the emission, and concluded that the best fits were achieved with  $R_{\text{min}}$  values less than about  $2R_*$  and with wind absorption included. The authors state that their fits are insensitive to changes in  $R_{\text{min}}$  for  $R_{\text{min}} \lesssim 2R_*$  because the radius of radial optical depth unity  $R(\tau = 1) \equiv R_1 \gg 2R_*$  for most of the wavelength range of the spectrum.

By combining *ROSAT* x-ray observations with *EUVE* EUV observations of the B bright giant  $\epsilon$  Canis Majoris, Cohen et al. (1996) were able to place constraints on wind attenuation and temperature distribution. This was the first analysis of high-energy hot-star spectra with high enough resolution to resolve individual lines. Exploring one- and two-temperature models similar to those of Hillier et al. (1993) with and without absorption, they achieved their best fits using a power law temperature distribution including absorption. They suggest that their upper bounds on absorption are too low to be consistent with a coronal model, given the observed mass-loss rate, but are consistent with wind-shock models. Cohen, Cassinelli, & MacFarlane (1997a) also found evidence for wind attenuation in early-type, near-main-sequence B stars, but could not explain the observed x-ray luminosity with purely line-force-instability-driven shocks. With slightly higher resolution *ASCA* data, Cohen, Cassinelli, & Waldron (1997b) came to similar conclusions about the B0 V star  $\tau$  Scorpii. In general it seems that B star x-ray emission, particularly from the later types, may not fit in to the wind-shock scenarios proposed for O stars.

Berghoefer et al. (1996) used *ROSAT* observations of  $\zeta$  Puppis looking for variability. They identified a periodic fluctuation of  $\pm 6\%$  in an otherwise quite constant x-ray flux with a period of 0.7 days and correlated it with  $H_\alpha$  line profile variability. The low level of observed variability has important implications for wind-shock models. The x-ray flux from an individual shock would be highly variable, as the shock arises, propagates through regions of varying density, and decays. A large number of shocks must, therefore, be continually arising to explain the low level of variability in  $\zeta$  Puppis.

The latest generation of x-ray observatories, *XMM* and *Chandra*, have vastly improved spectral resolution compared to earlier telescopes. *Chandra* provides spectra with resolution exceeding  $\lambda/\Delta\lambda \sim 1000$  at some wavelengths, corresponding to a Doppler velocity of  $v = c(\Delta\lambda/\lambda) \approx 300 \text{ km s}^{-1}$ , where  $\Delta\lambda$  is the full width at half maximum (FWHM) of the instrumental response. X-ray emission lines formed in material embedded in the wind should extend to Doppler shifts of  $v \sim \pm v_\infty$ . Observed wind terminal velocities approach  $v_\infty = 3000 \text{ km s}^{-1}$ , implying  $\sim 20$  resolution elements for a velocity range of  $2v_\infty$ . *Chandra* and *XMM* spectra of O stars do, in fact, reveal broad, resolved line profiles (Schulz et al. 2000; Kahn et al. 2001; Cassinelli et al. 2001; Waldron & Cassinelli 2001).

The x-ray line emission comes primarily from highly ionized helium- and hydrogen-like atoms of heavy elements. Cassinelli et al. (2001) report strong He- $\alpha$  complexes from the helium-like ions S XV, Si XIII, Mg XI, Ne IX, and O VII, and strong isolated lines of Mg XII, Ne X, Fe XVII, O VIII, and N VII in *Chandra* observation of  $\zeta$  Puppis. Essentially the same lines are seen in the *XMM* spectrum (Kahn et al. 2001), and in a *Chandra* spectra of other stars (Schulz et al. 2000; Waldron & Cassinelli 2001).

There are two types of diagnostics that have been applied to high-resolution x-ray spectra of hot stars: line ratios, and line profile shapes and widths.

Line ratios (often between lines in He- $\alpha$  complexes of helium-like ions) provide information about the density, temperature and ultraviolet flux conditions where the lines are formed. In general, it is not possible to separate the effects of density and UV flux using line ratios alone, but modeling, plausibility arguments, and independent diagnostics can separately place constraints on the density and UV flux. Line ratios have been used to estimate UV flux in the region where the lines are formed, which in turn can be used to determine the radius at which the lines arise when combined with an assumed value for the photospheric luminosity in the UV (Schulz et al. 2000; Waldron & Cassinelli 2001; Cassinelli et al. 2001; Cohen et al. 2003).

Line profile widths and shapes carry information about the velocity distribution of x-ray emitting material. At the most basic level, the width of a line should be related to the terminal velocity of the wind. Since the wind may only reach its terminal velocity far from the star where wind density is low, however, there may be very little x-ray emitting material at velocities approaching  $v_\infty$ . The exact relationship between a measurement like the FWHM and  $v_\infty$  will depend on the velocity distribution of hot gas, the wind attenuation, and the thermal and turbulent contributions to the broadening. Observed line widths range from several hundred to  $\sim 1000 \text{ km s}^{-1}$  (HWHM), suggesting that thermal broadening, at least, will be unimportant (Schulz et al. 2000; Waldron & Cassinelli 2001; Cassinelli et al. 2001).

Only recently have high-resolution spectra opened up the possibility of exploring line profile shapes for their diagnostic potential. Both *XMM* (Kahn et al. 2001) and *Chandra* (Cassinelli et al. 2001) spectra of  $\zeta$  Puppis are available, and the widths and centroid shifts of several line profiles from each have been published. Presented here is the first quantitative analysis of x-ray line pro-

files from a hot star (preliminary results from this work are reported in Kramer, Cohen, & Owocki 2003a<sup>1</sup> and Kramer et al. 2003b<sup>2</sup>).

## 2. A spherically-symmetric wind model

Detailed modeling of line profile shapes requires solving the problem of radiation transport in the wind. The luminosity at a wavelength  $\lambda$  will be the spatial integral of the product of volume emissivity  $\eta_\lambda(r, \theta, \phi)$  (which has dimensions of energy per units time, volume and solid angle and is assumed to be isotropic) and absorption  $e^{-\tau_\lambda(r, \theta, \phi)}$  (unitless) over the whole wind, where  $\tau_\lambda(r, \theta, \phi)$  is the (unitless) optical depth along the observers line of sight to a given point  $(r, \theta, \phi)$ . Then

$$L_\lambda = 4\pi \int_{\phi=0}^{2\pi} \int_{\theta=0}^{\pi} \int_{r=R_*}^{\infty} \eta_\lambda(r, \theta, \phi) e^{-\tau_\lambda(r, \theta, \phi)} r^2 \sin \theta dr d\theta d\phi, \quad (2-1)$$

where  $R_*$  is the stellar radius. We chose to orient our coordinate system so that the observer is located far away at  $\theta = 0$ . The optical depth  $\tau$  must be found by evaluating a separate integral along the line of sight.

In this study, we have adopted the model developed by Owocki & Cohen (2001). This model is a spherically-symmetric parameterization of the wind geometry and kinematics. It is based on the predictions of wind-shock theory, but may be tuned to describe a variety of physical models by varying its four parameters. Assuming spherical symmetry and expressing our polar integral in terms of the direction cosine  $\mu$ , Equation 2-1 becomes

$$L_\lambda = 8\pi^2 \int_{\mu=-1}^1 \int_{r=R_*}^{\infty} \eta_\lambda(\mu, r) e^{-\tau(\mu, r)} r^2 dr d\mu. \quad (2-2)$$

As in many of the models discussing in section 1.3, the emission is assumed to be primarily due to recombination and collisional processes, which scale like density squared  $\rho^2$ . An extra factor of  $r^{-q}$ , with  $q$  being a tunable parameter, allows for spatial variation of the fraction of the wind hot enough to emit x-rays. Wind-shock theories predict that shock formation will not begin immediately at the photosphere, but at some radius  $R_o > R_*$  (Hillier et al. 1993), so we also allow for that. The wind velocity is assumed to be purely radial and purely a function of radius. The line, assumed to be of infinitesimal width, is emitted at rest wavelength  $\lambda_0$ , which becomes  $\lambda_0 [v(r) \cos(\theta)/c]$  in the observer's reference frame. Combining these assumptions, we

---

<sup>1</sup>Paper available from <http://arxiv.org/abs/astro-ph/0211550>.

<sup>2</sup>Paper available from <http://arxiv.org/abs/astro-ph/0212313>.

obtain the volume emissivity

$$\eta_\lambda(\mu, r) = \begin{cases} C\rho^2(r)r^{-q} \delta\left(\lambda - \lambda_0\left(1 - \frac{\mu v(r)}{c}\right)\right) & \text{if } r \geq R_0 \\ 0 & \text{if } r < R_0, \end{cases} \quad (2-3)$$

where  $C$  is an undetermined constant of proportionality. Owocki & Cohen adopt the velocity given by Equation 1-8, with  $\beta$  becoming another model parameter. The density is then given by Equation 1-10, and the emissivity becomes

$$\eta_\lambda(\mu, r) = \left(\frac{C\dot{M}^2}{16\pi^2 v_\infty^2}\right) \frac{r^{-q-4}}{\left(1 - \frac{R_*}{r}\right)^{2\beta}} \delta\left(\lambda - \lambda_0\left(1 - \frac{\mu v(r)}{c}\right)\right) \text{ for } r \geq R_0. \quad (2-4)$$

The optical depth is found by integrating the mass absorption coefficient  $\kappa$  times the density along the line of sight:  $\tau = \int \kappa \rho dl$ . It is assumed that  $\kappa$  is constant across the line and throughout the wind, though the value may vary with wavelength from line to line. The primary source of x-ray opacity is photoionization of atoms in the cool component of the wind. Since the star is opaque to x-rays, lines of sight intersecting the star are assigned infinite optical depths. The optical depth becomes

$$\tau(\mu, r) = \begin{cases} \infty & \text{if } p \leq 1 \text{ \& } z \leq \sqrt{1 - p^2}, \\ \tau_* \int_z^\infty \frac{dz'}{r'^2(1 - 1/r')^\beta} & \text{otherwise,} \end{cases} \quad (2-5)$$

where the impact parameter is  $p \equiv (r/R_*)\sqrt{1 - \mu^2}$ , the line-of-sight distance is  $z \equiv \mu r/R_*$ ,  $r' \equiv \sqrt{p^2 + z'^2}$ , and several constants have been combined into

$$\tau_* \equiv \frac{\kappa \dot{M}}{4\pi v_\infty R_*}. \quad (2-6)$$

This relates to the commonly-quoted radius of optical depth unity  $R_1$  (for  $\beta = 1$ ) by the equation

$$\frac{R_1}{R_*} = \frac{1}{1 - \exp(-1/\tau_*)} \approx \tau_* + 0.5 \text{ for } \tau_* > 0.5. \quad (2-7)$$

The error in the above approximation is less than 10% for  $\tau_* > 0.67$  (or  $R_1/R_* > 1.3$ ).

The  $\delta$  function in Equation 2-4 lets us evaluate the angular integral in Equation 2-2. Defining

$$x \equiv \frac{c}{v_\infty} \left(\frac{\lambda}{\lambda_0} - 1\right), \quad (2-8)$$

the  $\delta$  function picks out the value of the integrand at  $\mu = x/(1 - R_*/r)^\beta$ :

$$L_x \propto \int_{r=r_x}^\infty \frac{r^{-(q+2)}}{\left(1 - \frac{R_*}{r}\right)^{3\beta}} \exp[-\tau(\mu_x, r)] dr, \quad (2-9)$$

where  $r_x \equiv \max [R_o, R_*/(1 - |x|^{(1/\beta)})]$  and  $\mu_x \equiv x/(1 - R_*/r)^\beta$ . For a discussion of the singularity at  $r = R_*$  see Appendix B.

The optical depth integral (eq. 2-5) may be solved analytically for integer values of  $\beta$ , but Equation 2-9 must be integrated numerically to obtain the line profile, except in the case of  $\beta = 0$  (constant velocity wind). In comparing the calculated profile to observations, determining the values of  $C$  and  $\dot{M}$  may be avoided by normalizing the line profile to predict the observed number of counts across the same wavelength range. The dependence on the value of  $R_*$  can be normalized out by expressing  $R_0$  in units of  $R_*$ . The model then depends on four parameters:  $\beta$ ,  $q$ ,  $R_0$ , and  $\tau_*$ .

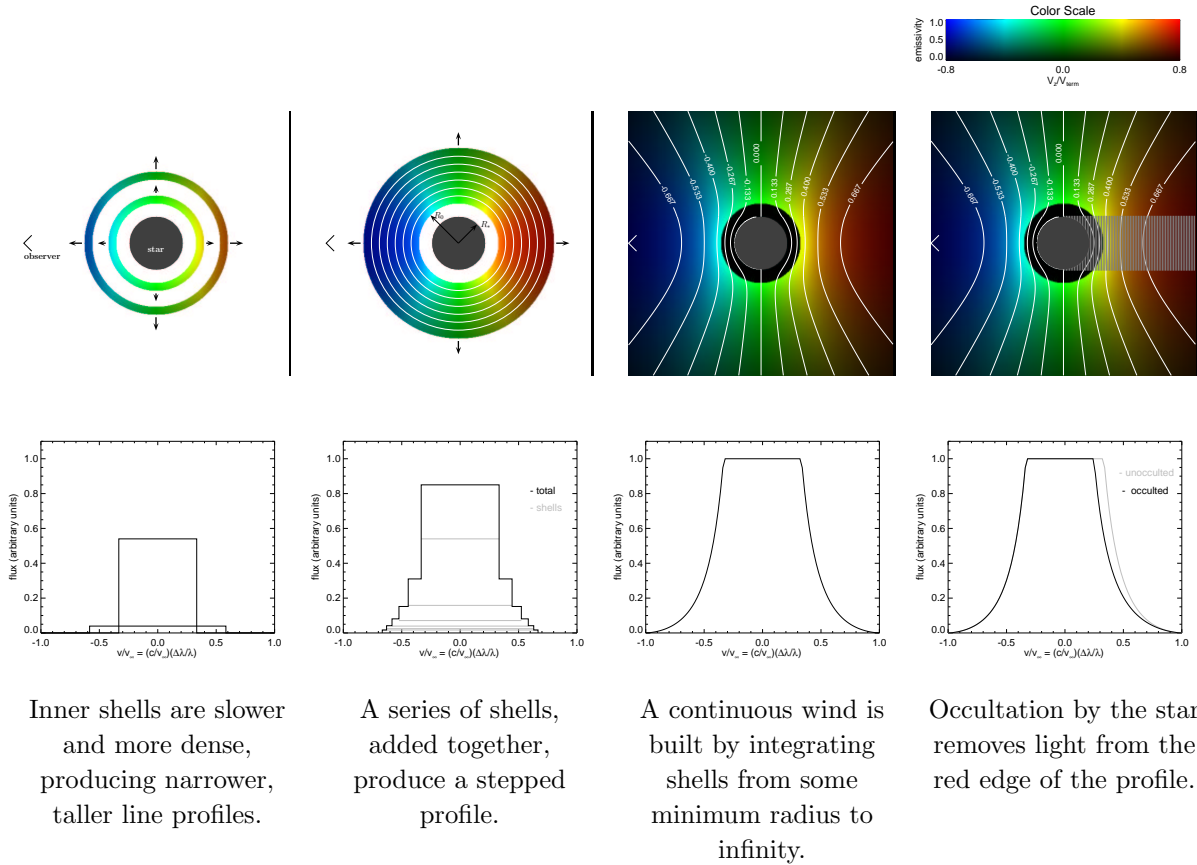


Fig. 1.— **Building a wind. Maps (top row):** Line-of-sight component of wind velocity for the observer to left of star ( $v_z$ , indicated by hue), and x-ray volume emissivity ( $\eta$ , brightness) is mapped in  $p$ - $z$  coordinates (impact-parameter versus line-of-sight distance). **Line profiles (bottom row):** Plots of flux (arbitrary scaling) versus wavelength (in velocity units scaled by  $v_\infty$ ) correspond to above maps. Bluest wavelengths are on the left, reddest on the right.

Without absorption, the profiles are flat-topped and symmetric (with sloping sides of a shape determined by the velocity law). Figure 1 graphically illustrates the process of building up a line profile from emission in the wind, which can be envisioned as integrating over a series

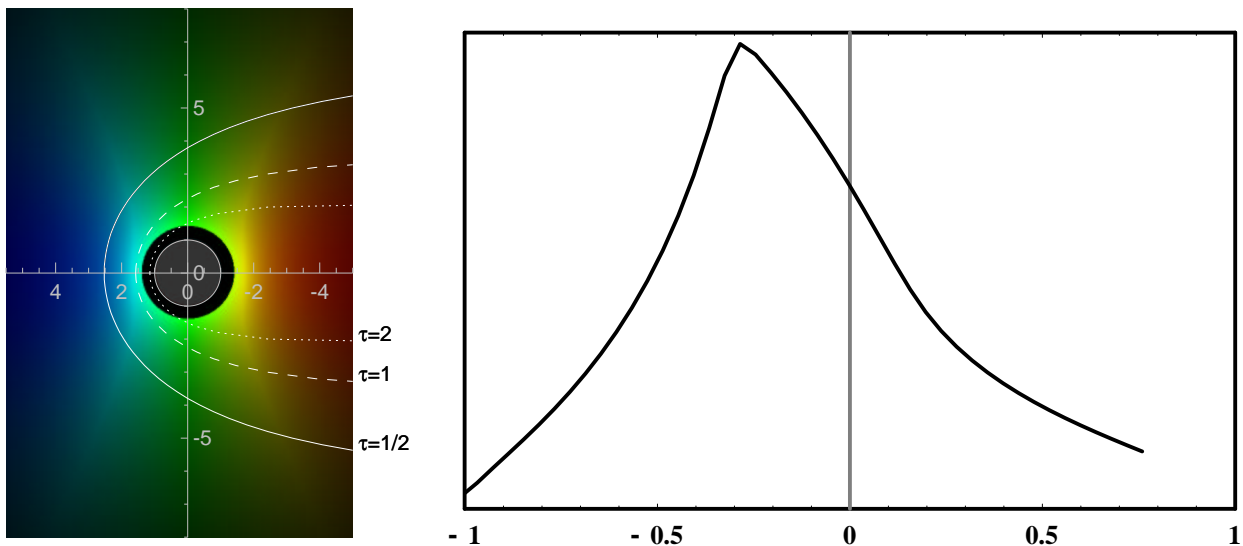


Fig. 2.— **Continuum absorption.** Contours of constant optical depth (integrated along the observer’s line of sight) overlay a wind map (left; see figure 1). The observer is to the left. The resulting line profile (right, not convolved with instrumental response function) shows the effect of an optically thick wind.

of infinitesimally-thin shells, each of which produces a rectangular profile with its width set by the shell velocity. Absorption (and occultation by the star) skews the line profile blueward by preferentially removing redder photons (see Figure 2).

Some other work has been done in the past using similar but less general treatments. In the context of EUV emission lines, MacFarlane et al. (1991) calculated the profile resulting from a single, thin spherical shock using similar arguments. He found that emission from a single shell produces a flat-topped rectangular line profile in the absence of absorption. Increasing the absorption (increasing the  $\tau_*$  parameter) preferentially decreases the flux at longer wavelengths, because the red-shifted photons tend to come from the far side of the star and pass through more wind material on the line of sight to the observer. Ignace (2001) found an analytic solution to equation 2-9 with  $\beta = 0$  (i.e. with a constant velocity wind  $v(r) = v_\infty$ ). Waldron & Cassinelli (2001) summed the flux from 10 spherical shocks with a distribution of velocities and emissivities to synthesize line profiles and compared them to *Chandra* observations of  $\zeta$  Orionis (O9.7 Ib), concluding that good correspondence to the observed profiles was only obtained in the limit of very little absorption due to the symmetry of the profiles.

The Owocki & Cohen (2001) treatment assumes opacity is constant across the wavelength range of the line. Opacity in the line itself has quite a different effect on the line profile. Ignace & Gayley (2002) have used the Sobolev approximation to treat line opacity in the constant-velocity case, deriving an analytical description of the profile shape in the high- $\tau_*$ , optically-

thick-line limit. They predict that line opacity will reduce the blueward shift of the line centroid, making it more symmetric.

We will primarily be exploring models in the optically-thin-line limit with integer, non-zero values of  $\beta$ .  $\beta = 1$  is considered the most appropriate value given the typical O star value of  $\beta = 0.8$  determined from UV observations (Groenewegen, Lamers, & Pauldrach 1989), the determination by Puls et al. (1996) of the value  $\beta = 1.15$  for  $\zeta$  Puppis.

### 3. Line profile fitting

To accomplish the quantitative analysis of line profile shapes presented here, a suite of original tools was written in the *Mathematica*<sup>3</sup> programming language. This section outlines the techniques implemented in this software.

#### 3.1. The data set

The data set consists of the  $\pm 1$  order coadded MEG spectrum from a 67 ks observation of the O4f star  $\zeta$  Puppis first reported on by Cassinelli et al. (2001). The FWHM of the MEG spectral response is  $\Delta\lambda_{\text{MEG}} = 0.023 \text{ \AA}$  (*Chandra* X-Ray Center 2001)<sup>4</sup>. All the distinguishable lines in this spectrum are many times more broad, allowing their profiles to be well resolved. For our purposes a more useful measure of instrumental broadening is the width of a Gaussian response function scaled by the terminal velocity of the wind,  $\sigma_x$ .

$$\sigma = \frac{\Delta\lambda}{2.35} \tag{3-1}$$

$$\sigma_x = \frac{\sigma}{\lambda_0} \frac{c}{v_\infty} = \frac{\Delta\lambda}{2.35\lambda_0} \frac{c}{v_\infty} \tag{3-2}$$

All models are convolved with a Gaussian of standard deviation  $\sigma_x$  to simulate the instrumental broadening before being compared to spectral data. Table 2 lists the values of  $\sigma_x$  for each fit.

A key assumption of our fitting procedure is that the noise in the data set is described by a pure Poisson distribution and that there is no significant background flux. Visual inspection of the spectrum indicates that there is no substantial continuum contribution to the flux, and we expect no background for the sky or instrument. Global spectral modeling using standard thermal plasma emission codes by Raymond & Smith (1977) shows that the free-free and recombination continua are negligible for the plasma temperatures implied by these lines.

---

<sup>3</sup>*Mathematica* is published by Wolfram Research, <http://www.wolfram.com/>.

<sup>4</sup>The *Chandra* Proposers' Observatory Guide is available at <http://cxc.harvard.edu/udocs/docs/>.

### 3.2. Blends and limits

The breadth of the lines in this spectrum causes many of them to be contaminated by emission from neighboring lines. After eliminating triplets as unsuitable for fitting due to excessive blending, other potential blends were identified by visual inspection and by referring to the line strengths calculated by Mewe, Gronenschild, & van den Oord (1985) and those in the Astrophysical Plasma Emission Database (APED, Smith et al. 2001)<sup>5</sup>. A line with rest wavelength  $\lambda_0$  is considered to extend over a wavelength range defined by

$$\lambda_0 \left(1 + \frac{v_\infty}{c}\right) + \Delta\lambda_{\text{MEG}} \geq \lambda \geq \lambda_0 \left(1 - \frac{v_\infty}{c}\right) - \Delta\lambda_{\text{MEG}} . \quad (3-3)$$

The widths of neighboring lines are calculated the same way, and any overlap in the ranges is excluded from the fit. See Table 2 for the wavelength range over which each fit was performed, and appendix A for details of suspected blends. The terminal velocity value determined by Prinja et al. (1990)  $v_\infty = 2485 \text{ km s}^{-1}$  is adopted here.

### 3.3. Synthesizing line profiles

For a quantitative comparison between a given model and an observed line profile, the model must produce a predicted spectrum commensurate with the observational data. This is the algorithm implemented in *Mathematica* for this purpose:

1. Chose a set of values for the model parameters,  $\beta$ ,  $q$ ,  $R_o$ , and  $\tau_*$ .  $\beta$  must be an integer<sup>6</sup>  $\geq 0$ . Symbolically evaluate the optical depth integral (equation 2-5) to obtain an analytic expression for  $\tau$  as a function of  $\mu$  and  $r$ .
2. Chose a domain (a range of  $x$  values) over which to evaluate the line profile (see section 3.2). At a series of  $x$  coordinates (equation 2-8) within the domain, numerically integrate the radial integral in equation 2-9.
3. Convolve the resulting spectrum with a Gaussian of width  $\sigma_x$  (equation 3-2) which characterizes the instrumental broadening.
4. Normalize the convolved profile so it has unit area in the desired domain.
5. Integrate the normalized profile function across the wavelength range of each observational bin within the desired domain. Multiply the resulting binned profile function by the total number of counts observed within the domain to produce a model spectrum that predicts the same total number of counts.

---

<sup>5</sup>The Interactive GUIDE for ATOMDB is available at <http://obsvis.harvard.edu/WebGUIDE/>.

<sup>6</sup>*Mathematica* is capable of symbolically integrating equation 2-5 for integer values of  $\beta$ .

This predicted spectrum is a set of expectation values for the number of photons counted in each bin, which may then be directly compared with the data using an appropriate fit statistic.

### 3.4. Parameter estimation and confidence regions

#### 3.4.1. The maximum likelihood statistic

The Poisson distribution governs the probability of a photon arriving in a bin (spatial and/or spectral) during a given time interval. If  $e_i$  is the expectation value of the photon count in bin  $i$ , the probability that the observed count will be  $n_i$  is

$$P_{e_i}(n_i) = \frac{e_i^{n_i} e^{-e_i}}{n_i!} . \quad (3-4)$$

The probability of observing a particular set of  $N$  photon-count values  $n_i$  is the product of the probability for each bin.

$$P = \prod_{i=1}^N \frac{e_i^{n_i} e^{-e_i}}{n_i!} . \quad (3-5)$$

Cash (1979) showed that the likelihood ratio for this distribution generates the statistic

$$C = -2 \ln P = -2 \sum_i (n_i \ln e_i - e_i - \ln n_i!) , \quad (3-6)$$

which may be replaced with

$$C = 2 \sum_i (e_i - n_i \ln e_i) . \quad (3-7)$$

The set of model parameters  $a_0$  that minimizes  $C$  (so that  $C = C_{\min}$  at  $a_0$ ) obviously maximizes  $P$ , so it is considered the most likely parameter set, or the best fit.  $\Delta C = C - C_{\min}$  is distributed like  $\chi^2$  with  $M$  degrees of freedom, where  $M$  is the number of free parameters, and can be used like  $\Delta\chi^2$  to define confidence intervals (Cash 1979). The region of parameter space in which  $\Delta C$  is less than some value corresponding to the desired confidence level defines the confidence region of that probability. Tables of  $\Delta\chi^2$  for different confidence levels and degrees of freedom are given in Press, Teukolsky, Vetterling, & Flannery (1992, §15.6). Numerical simulations by Nousek & Shue (1989) and Yaqoob (1998) demonstrate the superiority of the  $C$  statistic for performing fits and determining confidence intervals. We have chosen  $C$  as our fit statistic, and determine our confidence regions using  $\Delta C$ . Figure 3 shows fits to two representative lines.

Table 1. Stellar properties determined or adopted for  $\zeta$  Puppis by various authors.

Reference	$M$ ( $M_{\odot}$ )	$R$ ( $R_{\odot}$ )	$L_{\text{bol}}/10^{39}$ ( $\text{erg s}^{-1}$ )	$T_{\text{eff}}$ (kK)	$\dot{M}/10^{-6}$ ( $M_{\odot} \text{ yr}^{-1}$ )	$v_{\infty}$ ( $\text{km s}^{-1}$ )	$L_{\text{x}}/10^{32}$ ( $\text{erg s}^{-1}$ )
Biegging et al. (1989)	(61)	(18)	(3.5)	(42)	5.0	(2400)	...
Sciortino et al. (1990)	52	17	2.63	41	(4.8)	2600	2.6
Prinja et al. (1991)	...	...	...	...	...	2485	...
Lamers & Leitherer (1993)	(59)	(16)	(3.9)	(42)	2.4	(2200)	...
Puls et al. (1996)	52.5	19	3.4	42	5.9	2250	...

Note. — Values in parentheses were not determined in the cited paper.

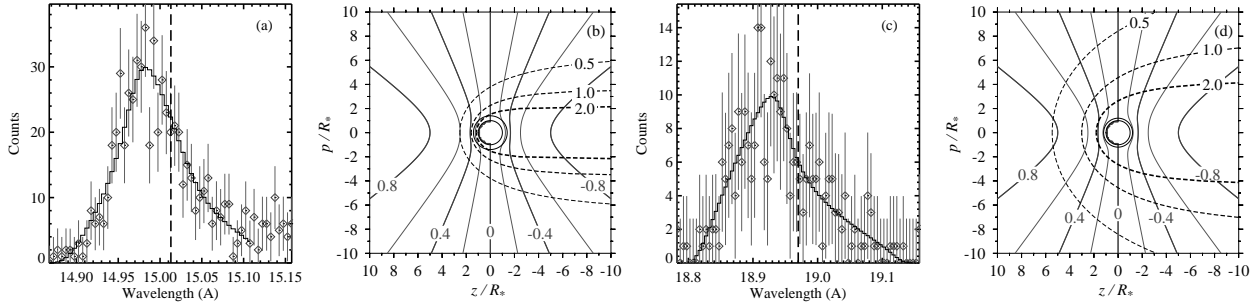


Fig. 3.— Two representative lines with best-fit models. Shown are *Chandra* MEG spectra of (a) Fe XVII at 15.01Å and (c) O VIII at 18.97Å (in gray), with corresponding best-fit profiles (in black). Laboratory rest wavelengths are indicated by the vertical dashed lines. To the right we show (b and d) contour plots representing the models. The observer is located at ( $p/R_* = 0, z/R_* = \infty$ ). The inner circle is of radius  $R_*$ , the outer circle of radius  $R_o$ . Gray contours are curves of constant line-of-sight velocity component in units of  $v_{\infty}$ . Dashed contours are curves of constant optical depth ( $\tau = 0.5, 1, 2$ ), integrated along the line of sight.

### 3.4.2. Mapping the fit statistic in parameter space

We use brute-force mapping of our fit statistic in parameter space to determine best-fit values and confidence intervals for the fit parameters. Since  $\beta$  is constrained to integer values, it is held constant for each fit, resulting in a three-dimensional parameter space. An inverted, unitless parameter

$$u_o \equiv R_*/R_o \tag{3-8}$$

was used in place of  $R_o$ . The algorithm for finding best-fit values and confidence regions is as follows.

1. Set up a 3-dimensional  $\{q, u_o, \tau_*\}$  grid in parameter space, with a fixed value of  $\beta$ .
2. At each point, calculate a model profile and the value of the fit statistic  $C$ .
3. Take the point with minimum value of  $C = C_{\min}$  to be the best-fit model  $a_0 = \{q, u_o, \tau_*\}|_{C=C_{\min}}$ .
4. Subtract  $C_{\min}$  from the grid of  $C$  values to obtain a grid of  $\Delta C$  values. All the points with  $\Delta C$  less than or equal to a given value are considered to be within the confidence region corresponding to that value.

In practice, the process usually involved multiple iterations: one or more low-resolution maps to get an approximate idea of the region of parameter space on which to focus followed by high resolution mapping to define confidence regions and identify the best-fit point. The step sizes of the final, high-resolution maps were standardized across all the fits for consistency. Some maps of small regions around the best-fit points were made at even higher resolutions, but  $C$  was always found to be a very shallow function of the model parameters, so this did not significantly improve the fits or tighten the confidence regions. This is not surprising, given that the model spectra vary slowly and smoothly with changes in the model parameters. One dimensional confidence intervals are simply the projections of the 3-D confidence regions. The validity of the confidence levels assigned to the regions was checked using Monte Carlo techniques.

Figure 4 shows a parameter-space map of confidence regions for the fit to the N VII line at 24.78 Å in the ζ Puppis spectrum. Each row of the figure consists of two panels. The left panels is a two-dimensional slice through the three-dimensional parameter space. These planes of constant  $\tau_*$  are color-coded to indicate which regions in the plane are contained within the 3-D confidence regions. The right panels plots the observed spectrum with the best-fit model *from that plane* in parameter space. Successive rows correspond to successive values of  $\tau_*$ . To demonstrate the typical range of models that can be fit to one line, Figure 5 shows the best-fit and two extreme models for the Fe XVII line at 17.05 Å. The two extreme models are for the parameter sets that have the largest and smallest values of  $\tau_*$  within the 95.4% confidence region.

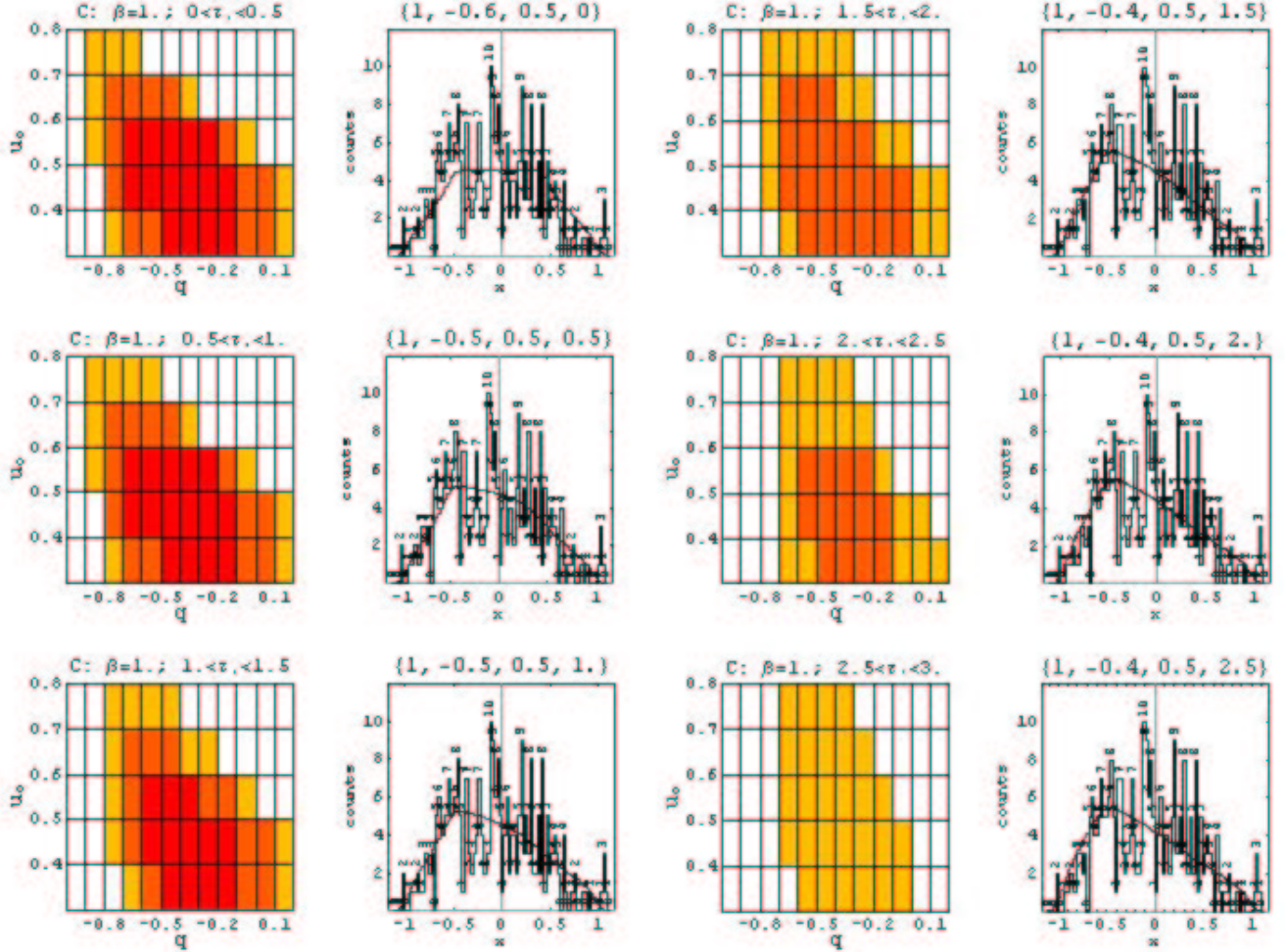


Fig. 4.— Projections of 3-D confidence regions and best-fit models in 2-D slices of parameter space. Red blocks in the grid are within the 68.3% confidence region, orange the 95.4% region, and yellow the 99.73% region. Values of  $\tau_*$  are indicated above the left-hand panes. The annotations above the right-hand panels indicate the values of the parameters  $\{\beta, q, u_0, \tau_*\}$  for the best-fit model within that plane. In the right-hand panes the model is plotted in red and the data in black. Note how the line profile changes with  $\tau_*$ : as the value increases the red side of the line is suppressed more and more. This fit is to the N VII line at 24.78 Å in the ζ Puppis spectrum. The overall best-fit occurs in the second row at  $\{1, -0.5, 0.5, 0.5\}$ .

### 3.5. Testing confidence levels with Monte Carlo simulations

Monte Carlo techniques can be used to test the validity of the confidence levels assigned to  $\Delta C$  contours. By simulating many data sets based on a single “best-fit” model, we can explore the sensitivity of the model parameters to random variations about the underlying distribution (Press et al. 1992, §15.6). The algorithm is outlined below:

1. Find set of parameters  $a_0$  that generate the best-fit model  $\mathcal{D}_0^S$  which minimizes the fit statistic.
2. Simulate many data sets  $\{\mathcal{D}_j^S\}$  based on the best-fit model:
  - (a) Synthesize an ideal spectrum (probability curve  $p(x)$ , where  $p(x)dx$  is the relative probability of a photon in the line being emitted with a scaled wavelength between  $x$  and  $x + dx$ ) using  $a_0$  and convolve it with the instrumental response function (a Gaussian of width  $\sigma_x$ ).
  - (b) Calculate the expectation value of the photons count for each bin by multiplying the total number of observed photons by the probability function integrated across each bin.
  - (c) Generate a set of  $N$  spectra  $\mathcal{D}_1^S \dots \mathcal{D}_N^S$  by randomizing the counts in each bin based on a Poisson distribution.
3. For each simulated spectrum  $\mathcal{D}_j^S$  calculate the value of the fit statistic (using  $\mathcal{D}_j^S$  as the “data” and the best fit  $\mathcal{D}_0^S$  as the “model”) on a small grid centered on  $a_0$  and record the coordinates of the minimum,  $a_j^S$ .

The result is a scatter of points in parameter space  $\{a_j^S\}$  representative of the distribution of parameter sets that might have produced the observed data. Arbitrarily-shaped confidence regions may be drawn to include the desired fraction of the points, or confidence regions determined by  $\Delta C$  may be tested by calculating the fraction of Monte-Carlo points within them (this is the technique used here). 1000 Monte-Carlo simulations were run to test the confidence regions of each fit, and all of the results were consistent with the confidence levels assigned using  $\Delta C$ . At the 95.4% confidence level, most of the confidence regions contained more than 96% of the M-C points. In most cases lowering the  $\Delta C$  value to tighten the confidence regions and bring the percentage of M-C points contained closer to 95.4% would have minimal effects on the confidence intervals. Therefore the  $\Delta C$  confidence regions are used.

### 3.6. Hypothesis testing and goodness-of-fit statistics

One disadvantage to using the  $C$  statistic is that there is no corresponding goodness-of-fit statistic like reduced  $\chi^2$ . In fact, there is no standard goodness-of-fit statistic for data with

Poisson noise (Mighell 1999). One alternative is to employ a variant of the non-parametric Kolmogorov-Smirnov test. The K-S statistic is calculated between the cumulative probability distributions of the data and the model. This can be applied in this case by considering a line profile (with area normalized to unity) to be a probability distribution governing the wavelengths of incoming photons.

The statistics  $D_+$  and  $D_-$  measure the extremes of the difference between the empirical cumulative distribution function (ECDF)  $E(x)$  and the predicted cumulative distribution  $P_c(x)$ :

$$D_+ \equiv \max [E(x) - P_c(x)] \quad , \quad (3-9)$$

$$D_- \equiv \max [P_c(x) - E(x)] \quad . \quad (3-10)$$

The K-S statistic is

$$D \equiv \max [D_+, D_-] \quad . \quad (3-11)$$

The K-S statistic has the disadvantage of deemphasizing variation at the extremes relative to variation in the middle of the distribution (Press et al. 1992). This is because both the ECDF and the predicted cumulative distribution must converge to 0 and 1 at either extreme. The Kuiper statistic  $V$  avoids this problem, as it is unchanged by cyclic permutations of the distributions:

$$V \equiv D_+ + D_- \quad . \quad (3-12)$$

Since  $P_c$  is a monotonically increasing function and  $E(x)$  is an increasing stepped function, we need only compare the distributions at the edges of the steps. The procedure used to calculate these statistics is as follows:

1. From the data set  $\mathcal{D}$ , form the empirical cumulative distribution function  $E(x)$ . This is a function of scaled wavelength  $x$  which steps up by a value  $n_i/N_{\text{obs}}$  at the wavelength of each bin  $x_i$  (where  $n_i$  is the number of photons counted in bin  $i$  and  $N_{\text{obs}}$  is the total number of observed photons).  $E(x)$  is a normalized cumulative probability distribution. Let  $E_i = E(x_i)$ .
2. Using the best-fit parameters, form the predicted cumulative distribution function  $P_c(x)$ . Let  $P_i = P_c(x_i)$ .
3. Calculate

$$D_+ = \max [E_i - P_i] \quad , \quad (3-13)$$

$$D_- = \max [P_i - E_{i-1}] \quad , \quad (3-14)$$

and from them,  $V$  and  $D$ .

There are approximate formulas (and tabulated values) for the significance levels of the Kuiper and K-S statistics under two conditions (Press et al. 1992; D’Agostino & Stephens 1986): (1) there are no model parameters estimated from the data, and (2) the distribution is continuous. Neither condition is met here, since (1) three parameters are being estimated, and (2) the data are binned by wavelength and so form a discrete distribution. For these reasons the canonical formulas vastly underestimate the significance of the observed variation from the best-fit models. Therefore we must resort to Monte-Carlo techniques to estimate the significance of our statistical values. By simulating a large number of data sets we may explore the frequency distribution of the Kuiper statistic. The significance level  $\alpha(V)$  is the probability that variations due to random noise will produce a value of the Kuiper statistic greater than  $V$ , so larger values of  $V$  indicate a “better” fit. Using Monte-Carlo simulations, we can estimate  $\alpha(V)$  as the fraction of MC data sets that give a value of the Kuiper statistic greater than  $V$ . There are actually two slightly different  $V$  distributions that can be obtained using MC techniques. The different procedures are outlined below:

**Calculating  $\alpha_0(V)$ :**

1. Generate a large number of MC simulated data sets  $\{\mathcal{D}_j^S\}$  based on the best-fit parameters  $a_0$  as described in §3.5.
2. Generate  $E_j(x)$  for each simulated data set and  $P_{c_0}(x)$  from the  $a_0$  model and calculate the Kuiper statistic. This generates a set of values of the Kuiper statistic  $V_j^{S_0}$ .
3. Let  $\alpha_0(V)$  be the fraction of the values in the set  $V_j^{S_0}$  greater than  $V$ .

**Calculating  $\alpha_{\text{RF}}(V)$ :**

1. Generate a large number of MC simulated data sets  $\{\mathcal{D}_j^S\}$  based on the best-fit parameters  $a_0$  as described in §3.5.
2. Perform the fitting procedure on each MC data set to yield a new set of best-fit parameters for each MC set  $\{a_j^S\}$  (also as described in §3.5).
3. Generate  $E_j(x)$  for each simulated data set and  $P_{c_j}(x)$  from the corresponding  $a_j$  model (rather than  $a_0$ ) and calculate the Kuiper statistic. This generates a set of values of the Kuiper statistic  $V_j^{\text{SRF}}$ .
4. Let  $\alpha_{\text{RF}}(V)$  be the fraction of the values in the set  $V_j^{\text{SRF}}$  greater than  $V$ .

In general we expect  $\alpha_{\text{RF}}(V) \leq \alpha_0(V)$ , since the fitting procedure should find a model that matches the simulated data set as well as or better than  $a_0$ . A model is rejected if  $\alpha \leq 0.05$ . High values of the significance  $\alpha \geq 0.95$  can indicate that the model is over-specified, i.e. that there is not enough information in the data to reliably estimate all the model parameters simultaneously.

### 3.7. Goodness-of-fit results

The variation in spectral resolution as a function of wavelength and the need to truncate the fit range to avoid blends can cause fits to vary in quality and in the usefulness of parameter constraints derived from them. Listed in Table 2 are the MEG instrumental resolution  $\lambda_0/\Delta\lambda$ , the ratio of the full terminal-velocity width to the FWHM of the instrumental broadening  $2v_\infty/\Delta v$  (which is a measure of how well-resolved a line is), the scaled wavelength range of the fit  $\{x_{\min}, x_{\max}\}$  (both of which should have absolute values of slightly greater than unity for an un-truncated fit), and the number of spectral bins within the range of the fit  $N_{\text{obs}}$ .

For each fit  $\alpha_0$  was calculated from the distribution of  $V$  values of 1000 Monte-Carlo simulations, and  $\alpha_{\text{RF}}$  from the distribution of  $V$  values of 100 simulations with refitting. The results are reported in Table 3.

The lines at 18.97 Å, 17.054 Å, 15.013 Å, 12.13 Å, and 6.18 Å show a trend in fit quality according to both Kuiper-statistic distributions. Lines at longer wavelengths are better resolved, are sampled by more bins, and yield higher-quality fits than lines at shorter wavelengths. These fits are formally good, though the high significance levels of the two longest-wavelength fits suggests that the model may be under-determined. Also, the results of the fit to the Si XIV line at 6.18 Å are somewhat suspect because of the low resolution at that wavelength, the small number of bins, and the failure to constrain the  $q$  parameter.

The lines at 24.78 Å, 16.787 Å, and 15.262 Å yield anomalously-poor fits when compared to the lines listed above. The value of  $\alpha_0 = 0.039$  for the 15.262 Å fit does not meet the criterion  $\alpha \geq 0.05$  for a formally-good fit. This line may be contaminated by the Fe XIX lines at 15.198 Å and 15.3654 Å (APED). The relatively-low significance values for the N VII line may simply be the result of random variation, or could be a sign that there are resolved spectral features not explained by this simple model. In any case, the fit is formally good. The 16.787 Å fit may also be affected by a blend with an Fe XIX line, this one at 16.718 Å. This would add flux to the blue edge of the line, increasing its skew and explaining the relatively high values of  $\tau_*$  and  $q$ .

### 3.8. Effect of terminal velocity uncertainty on estimated parameters

To explore the influence of uncertainty in the wind terminal velocity on the fit results, a fit with  $v_\infty = 2200 \text{ km s}^{-1}$  was performed on the Fe XVII line at 15.013 Angstroms. The changes to the best-fit values are insignificant, and the changes in the confidence regions are quite small, though the quality of the fit is worse for the lower value (see Table 3). It is concluded that varying the terminal velocity value by less than 10% is unlikely to significantly affect fit results.

## 4. Results and Discussion

### 4.1. Summary

In all, fits were performed on eight lines in the  $\zeta$  Puppis spectrum between 6.18 Å (Si XIV) and 24.78 Å (N VII). Table 2 gives the parameters of each fit. The fits were all performed with a fixed value of  $\beta = 1$ . The estimated values of the parameters  $q$ ,  $R_o$ , and  $\tau_*$  are listed in Table 3, and shown in Figure 6 (the values for the Si XIV line are not shown in the figure because it is at a much shorter wavelength and its parameter values are poorly constrained). The confidence limits given are at the 95.4% confidence level (the “ $2\sigma$ ” level for a Gaussian distribution).

All the fits but one (to the Fe XVII line at 15.262 Å) are formally good, according to both of the Monte-Carlo-determined, Kuiper-statistic significance levels. The fitting procedure also placed useful constraints on the values of the estimated parameters. This leads to the primary conclusion of this work, that this simple, spherically-symmetric wind model can, in fact, fit line profiles in the  $\zeta$  Puppis x-ray spectrum. The success of this model is an especially important result since this is the first attempt at quantitative analysis of the information contained in x-ray line profiles from a hot star.

### 4.2. Estimated parameters

The determined amount of wind attenuation is significantly smaller than what one might expect from a spherically-symmetric, smooth wind, given what is known about this star’s mass-loss rate and wind opacity. There have been various calculations of the wind optical depth (often expressed as the radius of optical depth unity) as a function of wavelength for this star. They range from values much bigger than what we derive here ( $7 < \tau_* < 30$  calculated by Hillier et al. 1993, using  $\dot{M} = 5.0 \times 10^{-6} M_\odot \text{ yr}^{-1}$ ,  $R_* = 19 R_\odot$ ,  $v_\infty = 2200 \text{ km s}^{-1}$ ), to values modestly bigger ( $4 < \tau_* < 8$  calculated by Cassinelli et al. 2001, using values from Lamers & Leitherer 1993:  $\dot{M} = 2.4 \times 10^{-6} M_\odot \text{ yr}^{-1}$ ,  $R_* = 16 R_\odot$ ,  $v_\infty = 2200 \text{ km s}^{-1}$ ). Note that Hillier et al. (1993) find different values for  $R_1$  depending on whether helium recombines or remains ionized in the outer wind, but at energies above 0.5 keV (where all of the lines presented here occur) there is little difference between the two scenarios. More recent stellar parameters determined by Puls et al. (1996) ( $\dot{M} = 5.9 \times 10^{-6} M_\odot \text{ yr}^{-1}$ ,  $R_* = 19 R_\odot$ , and  $v_\infty = 2250 \text{ km s}^{-1}$ ) agree well with the values used by Hillier et al. (1993), but would increase the Cassinelli et al. (2001)  $\tau_*$  values by a factor of 2, given the same opacity (see eq. 2-6).

If we accept the  $\tau_*$  values derived from our fits, then the disparity between those values and the ones mentioned above suggest that either the mass-loss rates or wind opacities are being overestimated in previous calculations. The mass-loss rate of  $\zeta$  Puppis is by now quite well established using UV absorption lines and H $\alpha$ , although improper ionization corrections or clumping could lead to systematic errors. The wind opacity determination seems much more uncertain,

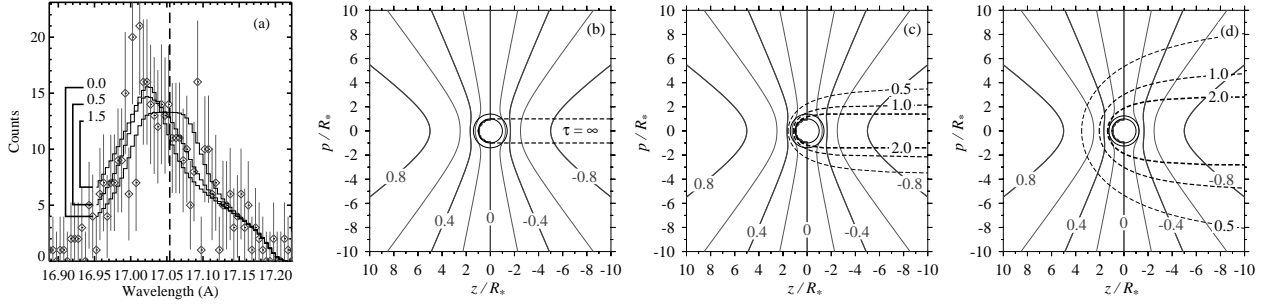


Fig. 5.— Models at extremes of the confidence region. Shown are the *Chandra* MEG spectrum of the 17.054 Å line of Fe XVII (in gray), and (in black) the best-fit model ( $\tau_* = 0.5$ ), the fit with  $\tau_*$  held at its 95.4% confidence upper limit ( $\tau_* = 1.5$ ) and the fit with  $\tau_*$  held at its 95.4% confidence lower limit ( $\tau_* = 0.0$ ). The contour plots are the same style as in Figure 3 and correspond to (b) the  $\tau_* = 0.0$  model, (c) the best-fit model, and (d) the  $\tau_* = 1.5$  model.

Table 2. Parameters of the line-profile fits.

Ion	$\lambda_0$ (Å)	$v_\infty$ (km s <sup>-1</sup> )	$\lambda_0/\Delta\lambda$	$2v_\infty/\Delta v$	$\sigma_x$	$x_{\min}$	$x_{\max}$	$N_{\text{obs}}$
N VII	24.78	2485	1077	18	0.048	-1.11	1.11	69
O VIII	18.97	2485	825	14	0.062	-1.04	1.14	92
Fe XVII	17.054	2485	741	12	0.069	-0.74	1.16	69
Fe XVII	16.787	2485	730	12	0.07	-1.16	0.74	54
Fe XVII	15.262	2485	664	11	0.077	-0.81	1.19	53
Fe XVII	15.013	2485	653	11	0.079	-1.19	0.79	50
Fe XVII	15.013	2200	653	10	0.089	-1.34	0.89	49
Ne X	12.13	2485	527	9	0.097	-1.23	0.03	49
Si XIV	6.18	2485	269	4	0.191	-0.98	0.59	26

Note. — The width of the instrumental response in wavelength units is  $\Delta\lambda = \Delta\lambda_{\text{MEG}} = 0.023$  Å, or in velocity units  $\Delta v = c\Delta\lambda/\lambda_0$ . The scaled wavelength  $x \equiv (c/v_\infty)(\lambda - \lambda_0)/\lambda_0$ .  $N_{\text{obs}}$  is the number of wavelength bins included in the fit.

Table 3. Estimated parameter values with 95.4% confidence intervals and goodness-of-fit calculations.

Ion	$\lambda_0$ (Å)	$v_\infty$ (km s <sup>-1</sup> )	$q$	$R_o/R_*$	$\tau_*$	$V$	$\alpha_0$	$\alpha_{\text{RF}}$
N VII	24.78	2485	$-0.5^{+0.6}_{-0.3}$	$2.0^{+1.3}_{-0.6}$	$0.5^{+2.0}_{-0.5}$	0.073	0.667	0.356
O VIII	18.97	2485	$-0.1^{+0.6}_{-0.4}$	$1.2^{+2.1}_{-0.2}$	$2.5^{+2.5}_{-1.5}$	0.066	0.941	0.790
Fe XVII	17.054	2485	$-0.6^{+0.4}_{-0.2}$	$1.4^{+0.6}_{-0.3}$	$0.5^{+1.0}_{-0.5}$	0.059	0.971	0.950
Fe XVII <sup>a</sup>	16.787	2485	$0.4^{+0.6}_{-0.6}$	$1.0^{+2.3}_{-0.0}$	$4.5^{+3.5}_{-2.5}$	0.087	0.517	0.490
Fe XVII <sup>a</sup>	15.262	2485	$-0.8^{+0.2}_{-0.2}$	$1.4^{+1.1}_{-0.4}$	$1.5^{+2.5}_{-1.5}$	0.095	0.039	0.151
Fe XVII	15.013	2485	$-0.2^{+0.4}_{-0.3}$	$1.4^{+0.6}_{-0.3}$	$1.0^{+1.0}_{-0.5}$	0.067	0.887	0.800
Fe XVII	15.013	2200	$-0.4^{+0.4}_{-0.2}$	$1.4^{+0.6}_{-0.4}$	$1.5^{+1.5}_{-1.0}$	0.078	0.562	0.370
Ne X	12.13	2485	$-0.4^{+0.5}_{-0.3}$	$1.4^{+0.6}_{-0.4}$	$1.0^{+1.5}_{-1.0}$	0.106	0.432	0.100
Si XIV <sup>b</sup>	6.18	2485	$-0.2^{+\dots}_{-0.8}$	$1.4^{+8.6}_{-0.4}$	$1.5^{+5.5}_{-1.5}$	0.148	0.857	0.622

<sup>a</sup>The anomalous results for these lines may be due to contamination. See §3.7.

<sup>b</sup>At the 95.4% confidence level upper limit,  $q$  is unconstrained for this fit.

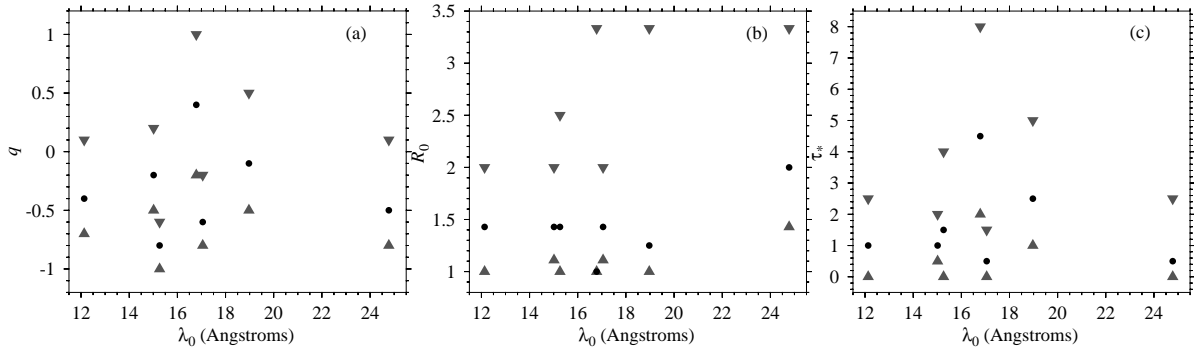


Fig. 6.— The best-fit values of (a)  $q$ , (b)  $R_o$ , and (c)  $\tau_*$  for seven of the eight fitted lines in the  $\zeta$  Puppis spectrum (bullets), along with the range given by the 95.4% confidence limits (triangles). See Table 3.

both because of the inconsistent values in the literature and because of the difficulty in determining the ionization state of the wind (Macfarlane et al. 1993; Macfarlane, Cohen, & Wang 1994). Recent advances in stellar atmosphere modeling may help to improve these determinations (Pauldrach, Hoffmann, & Lennon 2001). Another means of lowering the wind attenuation is to clump the wind into small clouds that are individually optically thick rendering the wind porous and enhancing the escape probability of x-ray photons, thus lowering the mean wind opacity. This would also affect the mass-loss rate diagnostics, but is, itself, an independent effect. Feldmeier et al. (2002b), Oskinova, Feldmeier, & Hamann (2002), and Feldmeier, Oskinova, & Hamann (2002a)<sup>7</sup> have done work on how such clumping might arise and how it might affect observed x-ray spectra.

An even more curious result of the  $\tau_*$  fits is that they are nearly independent of wavelength. This is surprising because photoionization cross sections should scale roughly as a power of wavelength between  $\lambda^2$  and  $\lambda^3$  (Hillier et al. 1993). It is possible that the distribution of ionization edges could conspire to make this relationship much flatter over a small range of wavelengths (as the calculations from Cassinelli et al. 2001 seem to indicate). But wind clumping might play some role, here too. If the wind opacity is dominated by clumps that are individually optically thick across the wavelength range, then the opacity ceases to be a function of wavelength and instead depends on the physical cross sections of the clumps themselves. Note that the UV line opacity necessary to explain the observed absorption line profiles could, in principle, still be provided by the tenuous inter-clump wind, as the line cross sections are much bigger than the x-ray photoionization cross sections.

If  $R_1 \gg R_o$ , the line profile is insensitive to changes in  $R_o$ , since emission much below  $R_1$  is largely absorbed by the wind. The values we find for  $R_o$ , though generally small, are comparable to our values of  $R_1$  (from  $\tau_*$  by eq. 2-7). It is hard to assess these relatively small onset radii in the context of the small (sometimes surprisingly small) values claimed on the basis of observed  $f/i$  ratios in He-like ions (Cassinelli et al. 2001; Kahn et al. 2001; Waldron & Cassinelli 2001). This is partially because we do not fit the profiles of any He-like lines (they are too blended) and partly because the most extreme result (smallest value for  $R_1$ ) from the line ratios is for S XV, which is a higher ionization stage than any of the lines we fit. The constraints we were able to place on  $R_1$ , though, suggest that the onset of shock formation is fairly close to the photosphere.

The fit results for the parameter  $q$  indicate that there is not a strong radial trend in the filling factor. One might expect some competition in a wind shock model between the tendency to have more and stronger shocks near the star, where the wind is still accelerating, and the tendency for shock heated gas to cool less efficiently in the far wind, where densities are low. Perhaps these two effects cancel to give the observed  $q \approx 0$  relationship.

The radial variation of the emissivity is undoubtedly more complicated than is allowed for

---

<sup>7</sup>These papers are available at <http://auriga.astro.physik.uni-potsdam.de/~afeld/publications.html>.

by the simple assumptions of this model, but in the absence of additional empirical information and in the interest of simplicity, the decision was made to attempt fits using a single radial power law. The quality of the fits justifies this choice to some extent.

From a theoretical point of view, we are already assuming emission arises in a large number of shocks which are, on some scale, distributed “smoothly” throughout the wind (this is supported by the variability observations of Berghoefer et al. 1996, as discussed in §1.3). We may then regard the wind as a two-component fluid, the bulk of which is cold X-ray absorbing material with a small fraction of embedded X-ray emitting plasma. Each individual shock will contain material at a range of temperatures controlled by the shock velocity and cooling structure, but on the scale at which the wind may be regarded as a two-component fluid it does not seem unreasonable to assume that these variations will also blend into a smooth, radial distribution.

## 5. Conclusion

The primary result of the analysis presented here is that x-ray emission lines in the prototypical O supergiant  $\zeta$  Puppis, can be adequately fit with a spherically-symmetric wind model having a small number of free parameters. The derived values of the parameters are quite reasonable in the context of most wind-shock models, being consistent with hot plasma uniformly distributed throughout the wind above a moderate onset radius, x-ray emission extending out to the wind terminal velocity, and the need for the inclusion of some wind attenuation. This provides the most direct evidence yet that some type of wind-shock model applies to this hot star. However, there are indications that the absorption properties of the wind of  $\zeta$  Puppis, and perhaps other hot stars, must be reconsidered.

In the future this model will be fit to *Chandra* spectra of other hot stars, but the lack of strong line asymmetries in stars such as  $\zeta$  Ori and  $\delta$  Ori and the narrow lines in  $\theta^1$  Ori C and  $\tau$  Sco indicate that spherically-symmetric wind-shock models with absorption may not fit the data from these stars as well as they do  $\zeta$  Puppis. The detection of a 1 kG magnetic field on  $\theta^1$  Ori C (Donati et al. 2002) and preliminary theoretical work on the effect of magnetic confinement of the wind on line profiles (Kramer et al. 2003b) suggests that the presence or absence of a strong, dipole magnetic field may separate hot stars into two classes: those without a strong field would have spherically symmetric winds and  $\zeta$  Puppis-type x-ray line profiles, while those with strong fields would have magnetically confined winds with narrower line profiles (at least from some viewing angles).

## Acknowledgements

I would like to acknowledge grant GO0-1089A to Swarthmore College and Prism Computational Sciences and funding provided by a Howard Hughes Medical Institute undergraduate

research grant. Stan Owocki and Elliot Reed did initial work on the Mathematica code used here. Rolf-Peter Kudritzki made valuable comments as referee of Kramer et al. (2003a). Eric Feigelson and Eric Jensen gave invaluable advice about goodness-of-fit tests. David Cohen has been an extremely patient and supportive advisor.

## A. Identified blends

This appendix lists all the potential blends identified in the lines considered for fitting in the  $\zeta$  Puppis spectrum (see APED).

### Si XIV 6.18 Å (H like)

No blends.

### Ne X 12.13 Å (H like)

Blend at  $\lambda = 12.285$  Å.

$$\lambda(1 - \frac{v_\infty}{c}) = 12.156, \lambda(1 - \frac{v_\infty}{c}) - \Delta\lambda_{\text{MEG}} = 12.133$$

### Fe XVII 15.013 Å (Ne like)

Blend at  $\lambda = 15.262$  Å.

$$\lambda(1 - \frac{v_\infty}{c}) = 15.135, \lambda(1 - \frac{v_\infty}{c}) - \Delta\lambda_{\text{MEG}} = 15.112$$

### Fe XVII 15.262 Å (Ne like)

Blend at  $\lambda = 15.013$  Å.

$$\lambda(1 + \frac{v_\infty}{c}) = 15.137, \lambda(1 + \frac{v_\infty}{c}) + \Delta\lambda_{\text{MEG}} = 15.16$$

Possible unaccounted-for blends at 15.198 Å and 15.3654 Å.

### Fe XVII 16.787 Å (Ne like)

Blend at  $\lambda = 17.054$  Å.

$$\lambda(1 - \frac{v_\infty}{c}) = 16.913, \lambda(1 - \frac{v_\infty}{c}) - \Delta\lambda_{\text{MEG}} = 16.89$$

Possible unaccounted-for blend at 16.718 Å.

### Fe XVII 17.054 Å (Ne like)

Blend at  $\lambda = 16.787$  Å.

$$\lambda(1 + \frac{v_\infty}{c}) = 16.926, \lambda(1 + \frac{v_\infty}{c}) + \Delta\lambda_{\text{MEG}} = 16.949$$

### O VIII 18.97 Å (H like)

Possible blend at  $\lambda = 18.63$  Å.

$$\lambda(1 + \frac{v_\infty}{c}) = 18.784, \lambda(1 + \frac{v_\infty}{c}) + \Delta\lambda_{\text{MEG}} = 18.807$$

## N VII 24.780 Å (H like)

No blends.

### B. Singularity in line profile integral

Equation 2-9 has an obvious singularity at  $r = R_*$ . This value only occurs at the low endpoint of the integral when  $x = 0$  and  $R_o = R_*$  and thus  $r_x = R_*$ . The singularity does not pose a problem except when  $\tau_*$  is less than about 1, and even so, the numerical integration package in Mathematica still gives a value, but warns about the singularity. The value of the integral at  $x = 0$  as we approach  $R_o = R_*$  from above converges smoothly to the one returned by Mathematica at  $R_o = R_*$ , which makes physical sense, so we have not seen the need for more formal exploration of the convergence.

### References

*In the online PDF version of this document, each reference is followed by a hyperlink to the online version of the resource, if it exists. Links to the NASA Astrophysics Data System<sup>8</sup> are designated by “[ADS]”, other links by “[LINK]”.*

Babel, J. 1995, A&A, 301, 823 [ADS]

Babel, J. & Montmerle, T. 1997, A&A, 323, 121 [ADS]

Berghoefer, T. W., Baade, D., Schmitt, J. H. M. M., Kudritzki, R.-P., Puls, J., Hillier, D. J., & Pauldrach, A. W. A. 1996, A&A, 306, 899 [ADS]

Biegging, J. H., Abbott, D. C., & Churchwell, E. B. 1989, ApJ, 340, 518 [ADS]

Cash, W. 1979, ApJ, 228, 939 [ADS]

Cassinelli, J. P., Miller, N. A., Waldron, W. L., MacFarlane, J. J., & Cohen, D. H. 2001, Astrophys. J. Lett., 554, L55 [ADS]

Cassinelli, J. P. & Olson, G. L. 1979, ApJ, 229, 304 [ADS]

Castor, J., McCray, R., & Weaver, R. 1975a, ApJ, 200, L107 [ADS]

Castor, J. I., Abbott, D. C., & Klein, R. I. 1975b, ApJ, 195, 157 [ADS]

---

<sup>8</sup>The ADS is online at <http://adswww.harvard.edu/>.

- Chandra* X-Ray Center. 2001, The *Chandra* Proposers' Observatory Guide, v4.0 edn., The *Chandra* X-Ray Center, Harvard-Smithsonian Center for Astrophysics, 60 Garden Street, Cambridge, MA 02138 USA [LINK]
- Chen, W. & White, R. L. 1991, ApJ, 366, 512 [ADS]
- Chlebowski, T., Harnden, F. R., & Sciortino, S. 1989, ApJ, 341, 427 [ADS]
- Cohen, D. H., Cassinelli, J. P., & MacFarlane, J. J. 1997a, ApJ, 487, 867 [ADS]
- Cohen, D. H., Cassinelli, J. P., & Waldron, W. L. 1997b, ApJ, 488, 397 [ADS]
- Cohen, D. H., Cooper, R. G., MacFarlane, J. J., Owocki, S. P., Cassinelli, J. P., & Wang, P. 1996, ApJ, 460, 506 [ADS]
- Cohen, D. H., de Messières, G. E., MacFarlane, J. J., Miller, N. A., Cassinelli, J. P., Owocki, S. P., & Liedahl, D. A. 2003, ApJ, 586, 495 [ADS]
- D'Agostino, R. B. & Stephens, M. A. 1986, Goodness-of-fit techniques (New York: Marcel Dekker) [ADS]
- Donati, J.-F., Babel, J., Harries, T. J., Howarth, I. D., Petit, P., & Semel, M. 2002, Mon. Not. R. Astron. Soc., 333, 55
- Feldmeier, A., Oskinova, L., & Hamann, W. R. 2002a, A&A, in press
- Feldmeier, A., Oskinova, L., Hamann, W. R., & Owocki, S. 2002b, in A massive star odyssey, IAU Symp. 212, ed. van der Hucht K., Herrero A., Esteban C. [LINK]
- Feldmeier, A., Puls, J., & Pauldrach, A. W. A. 1997, A&A, 322, 878 [ADS]
- Gagné, M., Caillault, J., Stauffer, J. R., & Linsky, J. L. 1997, ApJ, 478, L87+ [ADS]
- Groenewegen, M. A. T., Lamers, H. J. G. L. M., & Pauldrach, A. W. A. 1989, A&A, 221, 78 [ADS]
- Harnden, F. R., Branduardi, G., Gorenstein, P., Grindlay, J., Rosner, R., Topka, K., Elvis, M., Pye, J. P., & Vaiana, G. S. 1979, ApJ, 234, L51 [ADS]
- Hillier, D. J., Kudritzki, R. P., Pauldrach, A. W., Baade, D., Cassinelli, J. P., Puls, J., & Schmitt, J. H. M. M. 1993, A&A, 276, 117 [ADS]
- Howarth, I. D. & Prinja, R. K. 1989, ApJS, 69, 527 [ADS]
- . 1996, Ap&SS, 237, 125 [ADS]
- Ignace, R. 2001, ApJ, 549, L119 [ADS]

- Ignace, R. & Gayley, K. G. 2002, *ApJ*, 568, 954 [ADS]
- Kahn, S. M., Leutenegger, M. A., Cottam, J., Rauw, G., Vreux, J.-M., den Boggende, A. J. F., Mewe, R., & Güdel, M. 2001, *A&A*, 365, L312 [ADS]
- Kramer, R. H., Cohen, D. H., & Owocki, S. P. 2003a, *Astrophys. J. Letters*, submitted [LINK]
- Kramer, R. H., Tonnesen, S. K., Cohen, D. H., Owocki, S. P., Ud-Doula, A., & Macfarlane, J. J. 2003b, *Review of Scientific Instruments*, 74, 1966 [ADS]
- Kudritzki, R. & Puls, J. 2000, *ARA&A*, 38, 613 [ADS]
- Kudritzki, R. P., Palsa, R., Feldmeier, A., Puls, J., & Pauldrach, A. W. A. 1996, in *Roentgenstrahlung from the Universe*, ed. Zimmermann, H. U., Trümper, J. and Yorke, H. (Max-Planck-Institut für extraterrestrische Physik, Report 263), 9–12 [ADS]
- Kwok, S., Purton, C. R., & Fitzgerald, P. M. 1978, *ApJ*, 219, L125 [ADS]
- Lamers, H. J. G. L. M. & Cassinelli, J. P. 1999, *Introduction to stellar winds* (Cambridge: Cambridge University Press, 1999. ISBN 0521593980) [ADS]
- Lamers, H. J. G. L. M., Haser, S., de Koter, A., & Leitherer, C. 1999, *ApJ*, 516, 872 [ADS]
- Lamers, H. J. G. L. M. & Leitherer, C. 1993, *ApJ*, 412, 771 [ADS]
- Leitherer, C., Chapman, J. M., & Koribalski, B. 1995, *ApJ*, 450, 289 [ADS]
- Leitherer, C. & Lamers, H. 1993, *Space Science Reviews*, 66, 153 [ADS]
- Lucy, L. B. 1982, *ApJ*, 255, 286 [ADS]
- Lucy, L. B. & Solomon, P. M. 1970, *ApJ*, 159, 879 [ADS]
- Lucy, L. B. & White, R. L. 1980, *ApJ*, 241, 300 [ADS]
- MacFarlane, J. J. & Cassinelli, J. P. 1989, *ApJ*, 347, 1090 [ADS]
- MacFarlane, J. J., Cassinelli, J. P., Welsh, B. Y., Vedder, P. W., Vallergera, J. V., & Waldron, W. L. 1991, *ApJ*, 380, 564 [ADS]
- Macfarlane, J. J., Cohen, D. H., & Wang, P. 1994, *ApJ*, 437, 351 [ADS]
- Macfarlane, J. J., Waldron, W. L., Corcoran, M. F., Wolff, M. J., Wang, P., & Cassinelli, J. P. 1993, *ApJ*, 419, 813 [ADS]
- Mewe, R., Gronenschild, E. H. B. M., & van den Oord, G. H. J. 1985, *A&AS*, 62, 197 [ADS]
- Mighell, K. J. 1999, *ApJ*, 518, 380 [ADS]

- Mullan, D. J. 1984, *ApJ*, 283, 303 [ADS]
- Nousek, J. A. & Shue, D. R. 1989, *ApJ*, 342, 1207 [ADS]
- Oskinova, L., Feldmeier, A., & Hamann, W. R. 2002, in *A massive star odyssey*, IAU Symp. 212, ed. van der Hucht K., Herrero A., Esteban C. [LINK]
- Owocki, S. P. 2001, in *Encyclopedia of Astronomy and Astrophysics*, ed. Murdin, Paul (London: Nature Publishing Group), 2248–2256
- Owocki, S. P., Castor, J. I., & Rybicki, G. B. 1988, *ApJ*, 335, 914 [ADS]
- Owocki, S. P. & Cohen, D. H. 1999, *ApJ*, 520, 833 [ADS]
- . 2001, *ApJ*, 559, 1108 [ADS]
- Pauldrach, A. W. A., Hoffmann, T. L., & Lennon, M. 2001, *A&A*, 375, 161 [ADS]
- Press, W. H., Teukolsky, S. A., Vetterling, W. T., & Flannery, B. P. 1992, *Numerical recipes in C. The art of scientific computing* (Cambridge: University Press, 1992, 2nd ed.) [ADS]
- Prinja, R. K., Barlow, M. J., & Howarth, I. D. 1990, *ApJ*, 361, 607 [ADS]
- . 1991, *ApJ*, 383, 466 [ADS]
- Puls, J., Kudritzki, R.-P., Herrero, A., Pauldrach, A. W. A., Haser, S. M., Lennon, D. J., Gabler, R., Voels, S. A., Vilchez, J. M., Wachter, S., & Feldmeier, A. 1996, *A&A*, 305, 171 [ADS]
- Raymond, J. C. & Smith, B. W. 1977, *ApJS*, 35, 419 [ADS]
- Schulz, N. S., Canizares, C. R., Huenemoerder, D., & Lee, J. C. 2000, *ApJ*, 545, L135 [ADS]
- Sciortino, S., Vaiana, G. S., Harnden, F. R., Ramella, M., Morossi, C., Rosner, R., & Schmitt, J. H. M. M. 1990, *ApJ*, 361, 621 [ADS]
- Seward, F. D., Forman, W. R., Giacconi, R., Griffiths, R. E., Harnden, F. R., Jones, C., & Pye, J. P. 1979, *ApJ*, 234, L55 [ADS]
- Smith, R. K., Brickhouse, N. S., Liedahl, D. A., & Raymond, J. C. 2001, *ApJ*, 556, L91, APED [ADS]
- Sobolev, V. V. 1960, *Moving envelopes of stars* (Cambridge: Harvard University Press, 1960) [ADS]
- ud-Doula, A. & Owocki, S. P. 2002, *ApJ*, 576, 413 [ADS]
- Waldron, W. L. & Cassinelli, J. P. 2001, *ApJ*, 548, L45 [ADS]
- Yaqoob, T. 1998, *ApJ*, 500, 893 [ADS]

